Micron 133 (2020) 102863

Contents lists available at ScienceDirect

Micron

journal homepage: www.elsevier.com/locate/micron

Image-analysis based readout method for biochip: Automated quantification of immunomagnetic beads, micropads and patient leukemia cell

Fatma Uslu[a], Kutay Icoz[a,b,c,*], Kasim Tasdemir[c], Refika S. Doğan[a,b], Bulent Yilmaz[a,b,c]

[a] BioMINDS (Bio Micro/Nano Devices and Sensors) Lab, Electrical and Electronics Engineering Department, Abdullah Gül University, Kayseri, 38080, Turkey
[b] Bioengineering Department, Abdullah Gül University, Kayseri, 38080, Turkey
[c] Computer Engineering Department, Abdullah Gül University, Kayseri, 38080, Turkey

ARTICLE INFO

Keywords:
Biochip
Image processing
Leukemia cells
Micropads
Immunomagnetic beads
Bright-field optical microscope

ABSTRACT

For diagnosing and monitoring the progress of cancer, detection and quantification of tumor cells is utmost important. Beside standard bench top instruments, several biochip-based methods have been developed for this purpose. Our biochip design incorporates micron size immunomagnetic beads together with micropad arrays, thus requires automated detection and quantification of not only cells but also the micropads and the immunomagnetic beads. The main purpose of the biochip is to capture target cells having different antigens simultaneously. In this proposed study, a digital image processing-based method to quantify the leukemia cells, immunomagnetic beads and micropads was developed as a readout method for the biochip. Color, size-based object detection and object segmentation methods were implemented to detect structures in the images acquired from the biochip by a bright field optical microscope. It has been shown that manual counting and flow cytometry results are in good agreement with the developed automated counting. Average precision is 85 % and average error rate is 13 % for all images of patient samples, average precision is 99 % and average error rate is 1% for cell culture images. With the optimized micropad size, proposed method can reach up to 95 % precision rate for patient samples with an execution time of 90 s per image.

1. Introduction

During the cancer therapy, the detection and the quantification of tumor cells are required to monitor the progress of the treatment. Chemotherapy is one of the widely used standard treatment methods, however it has severe side effects, and it does not show the same effect on every patient e.g. refractory, relapse, complete remission (DeSantis et al., 2014; Sun et al., 2018). Personalized optimal dose of chemotherapeutics can minimize the risk of harmful toxicity and maximize the effectiveness of the treatment (Gao et al., 2008). Some cancer cells can be resistant to chemotherapy, and can cause relapses and repeat the cancer which is known as minimal residual disease (MRD) (Hauwel and Matthes, 2014). In order to monitor MRD and adjust the dosing of chemotherapeutics, flow cytometry (FC) and polymerase chain reaction (PCR) based molecular or immunological assays have been widely used (Böttcher et al., 2008; Neale et al., 2004). As an alternative to FC and PCR, microfluidic platforms have been developed (Jackson et al., 2016).

A large amount of data is produced when microscopes and attached cameras are used to record images from microfluidic chips, and powerful processors and algorithms are required to analyze the data (Faley et al., 2008). The techniques used to detect and segment microscopy and pathology images were reviewed broadly in (Xing and Yang, 2016). Compared to fluorescence (Mata et al., 2019), phase contrast and electron microscopy, unstained bright-field microscopy has the lowest cost and easiest method to implement. As a result of the optical properties of the cells, it is difficult to identify them in bright-field images (Georgantzoglou et al., 2015); to overcome this limitation, the cells are first stained and then automated image processing methods based on segmentation (Putzu et al., 2014) and thresholding (Hazwani et al., 2011) are applied. Fiji (Schindelin et al., 2012) and Icy (De Chaumont et al., 2012) are very useful open access software tools for image analysis, cell segmentation and cell detection. In addition, automated detection of cells from bright-field images was performed by machine learning-based methods (Long et al., 2006; Mualla et al., 2013). In (Long et al., 2006), non-living and living cells from bright-field images were detected by using support vector machines (SVM) method which includes training and test steps. In (Mualla et al., 2013), the detection of

* Corresponding author at: BioMINDS (Bio Micro/Nano Devices and Sensors) Lab, Electrical and Electronics Engineering Department, Abdullah Gül University, Kayseri, 38080, Turkey.
E-mail address: kutay.icoz@agu.edu.tr (K. Icoz).

https://doi.org/10.1016/j.micron.2020.102863
Received 16 January 2020; Received in revised form 5 March 2020; Accepted 19 March 2020
Available online 20 March 2020
0968-4328/

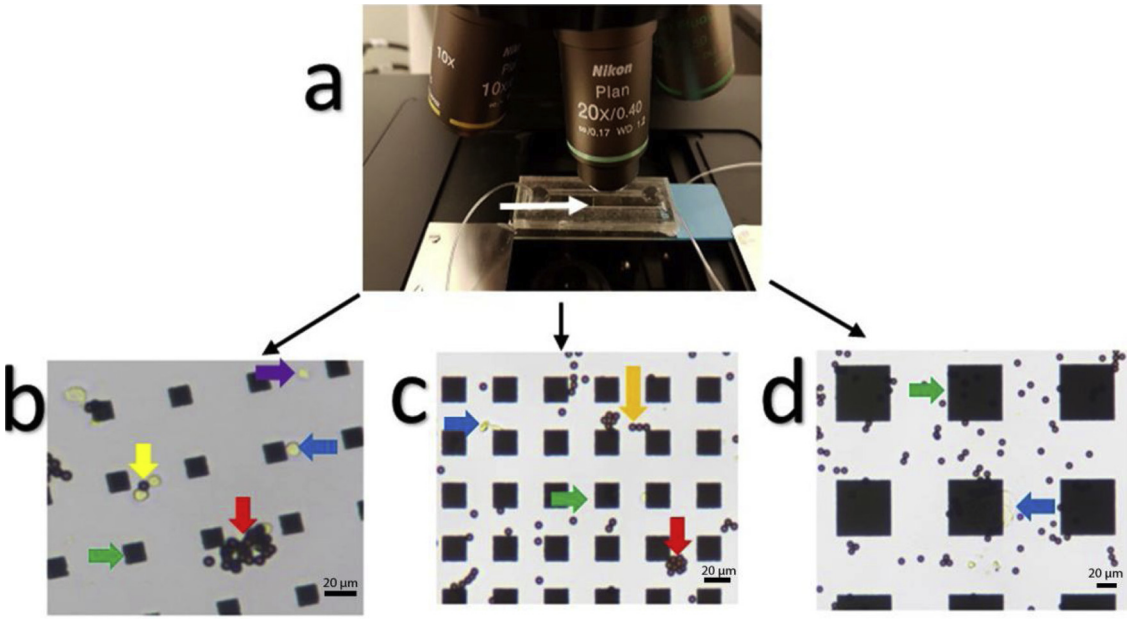

Fig. 1. a) Optical microscopy system with 20X objective and the microfluidic platform b) 20X objective biochip microscopy image which has small micropad. c) 20X objective biochip microscopy image which has bigger micropad areas than a. d) 20X objective biochip microscopy image which has larger micropad area than b and c. Blue arrow indicates cells attached to a micropad, purple arrow indicates a single cell, yellow arrow indicates two single cells with attached bead, red arrow indicates fully covered cells with beads as cluster, and green arrow indicates square pads. In addition, white arrow indicates the part of the biochip for capturing the image (For interpretation of the references to colour in this figure legend, the reader is referred to the web version of this article.).

unstained cells in bright-field microscopy images was achieved by scale-invariant feature transform (SIFT), random forests and hierarchical clustering. Automatically, unstained cell and vacuole segmentation and quantification in bright-field images were developed in (Chiang et al., 2018). Advanced level set, active contour or watershed methods, or combinations of them were applied for cell segmentation (Padfield et al., 2009; Tse et al., 2009; Li et al., 2007). Another open access image processing software is PIACG (Georg et al., 2018), which is able to estimate the total area of the viable cells in fetal bovine serum from the microscopy images of microfluidic chips. This software is Python based and it can detect and segment large number of unstained cells that are on uneven surfaces. The software also recognizes the objects that are not cells, such as the boundaries of the microfluidic channels. Generally, thresholding and filtering operations are performed in the image processing methods for this Python based software. PIACG does not require pre-processing steps, and is able to measure the cell area. However, it was proposed as a tool to quantify the area of a specific cell type in cell cultures. It is not capable of detecting and quantifying different cell types, and also other objects in the image.

In our previous work (Uslu et al., 2019), we have developed machine learning based image analysis algorithms to detect and quantify cells and immunomagnetic particles using bright-field microscopy images. We compared the impact of 20X and 40X objectives on the performance of the system. The images included only cells and immunomagnetic beads but not any microfabricated structures. We achieved 91.6 % precision for the images acquired with a 40X objective and 79.7 % precision for images acquired with a 20X objective. The average processing time for one image by using a computer which has Intel i7 – 7820HQ, 2.90 GHz processor and 8 GB RAM was found to be 300 s. We also have investigated the impact of the image quality on the performance of the algorithm such as precision and detection error.

In this study, we introduce an automated detection and quantification method as a readout mechanism of the microfluidic platform. The purpose of the microfluidic platform is to monitor the patient response to chemotherapy. The aim of the developed image processing algorithm is to be able to count patient leukemia cells, immunomagnetic beads and micropads from the images acquired by using a bright-field microscope with 20X objective. To reduce the processing time, we developed the image processing algorithm which benefit from color, size and shape identification. A maximum of 90 s is required to analyze a single image.

In the microfluidic platform, immunomagnetic beads and micropads were functionalized with different types of antibodies which enables screening target cells for multiple antigens in the cell membrane. In affinity-based biosensors, generally sandwich assays incorporating two antibodies are used. One antibody is immobilized on the surface as capture antibody and the second antibody is usually used as detection antibody (Masdor et al., 2017). In this study, the antibody functionalized micropads serve the purpose of capturing target cells in the microfluidic platform and thus, target cells were quantified.

2. Materials

2.1. Immunomagnetic capture of B lymphoblast cells

The details of the experimental procedure for capturing B lymphoblast cells were reported in our previous work (İçöz et al., 2019). Briefly two types of immunomagnetic beads (micron size CD19 antibody coated and nano size CD10 antibody coated) sequentially separated the target cells. The gold coated micropads in the biochip was functionalized with CD45 antibody by following the procedures reported in (Icoz et al., 2018). The separated target cells were introduced to the biochip, and the cells in the microfluidics were imaged for automated cell quantification.

2.2. Image acquisition and processing

Images were captured using a bright-field optical microscopy system, that includes DS-Ri 1 model CCD color camera and 20X objective (Nikon Instruments, Melville, NY). The captured images were of size 3116 × 4076 pixels. General view of the system is shown in Fig. 1.a. The system acquired images from the MRD biochip. The cells inside the MRD biochip were unstained and no fluorescent dyes were used.

Image analysis algorithms were developed on Matlab (R2018b, The MathWorks Inc., Natick, MA), running on PC system with Intel i7 − 7820HQ, 2.90 GHz CPU and 8 GB RAM on it.

To compare the results of manual counting and automated counting methods, SPSS software (IBM) was used for non-parametric Mann-Whitney *U* test

2.3. Ethical approval

This study was approved by the Clinical Research Ethics Committee of the Erciyes University Faculty of Medicine (Approval date: 09/01/2015, Decision no:2015/21, Kayseri, Turkey). Written informed consent was obtained from all patients or legally authorized representatives of patients. The Declaration of Helsinki was followed throughout the study.

3. Methods: Detection of micropads, immunomagnetic beads, cells and counting process

The purpose of the proposed methods is to count cells, immunomagnetic beads, and micropads in the images which are acquired by a bright-field microscopy with 20X objective (Fig. 1.a). In a typical image, there are 3 objects: cells, immunomagnetic beads and micropads (Fig. 1.b.c.d). Beads and micropads have uniform shapes and sizes whereas cells have various shapes and sizes (Long et al., 2006; Mualla et al., 2013). The fabrication of the micropads and manufacturing the microfluidic platform were explained in details in another article (manuscript submitted). We tested micropads in various sizes in order to determine the optimum micropad size for detection. In Fig. 1.b, the yellow arrow indicates that some cells and immunomagnetic beads are almost at the same size of 4.5 μm in diameter. Some cells in the images appear as isolated cells as in Fig. 1b, c, d by blue arrows, whereas some of them are fully or partially covered by immunomagnetic beads as in Fig. 1b, c, d (red and yellow arrows respectively). This means that, if immunomagnetic beads bind to the same cell and form a cluster, this cluster indicates an underlying cell even if the cell is not visible. However, all bead clusters do not always indicate an underlying cell, because magnetized immunomagnetic beads can attract to each other and form a chain like structures without covering any cell (Mzava et al., 2016a). An example of immunomagnetic beads in chain formation is shown in Fig. 1c indicated by an orange arrow. The developed algorithm considers clustered beads as an indicator of an underlying cell and chain like structures as beads only. All of the different situations are indicated in Fig. 1 with colored arrows.

The goal of the proposed algorithm is the precise detection and counting of immunomagnetic beads even though the beads might appear in various forms e.g. beads might bind to a cell, or to a micropad, beads might form a cluster or beads might appear as a floating single bead or a chain of beads (Fig. 1b, c, d).

In order to count beads and cells the algorithm has to identify micropads which might appear as a single micropad or a micropad that bound to cells/beads or both of them (Fig. 1b, c, d).

The afore mentioned cases are covered in the developed algorithm and explained in the next sections.

3.1. Micropad detection and quantification

Micropads have regular square shape and are placed in a grid order (Fig. 2). Micropad sizes can be different in each experiment depending on the production of the biochip. The micropads used in this study have sizes in between 15 μm x 15 μm–35 μm x 35 μm range. Micropads are larger than immunomagnetic beads and significantly opaquer than cells (Fig. 2b). Since our primary objective is to detect cells, we can identify micropads by considering the distinct features. This goal can easily be achieved by using morphological operations. It is known that, if closing operation is applied to the image with a structuring element larger than small objects, those small objects will be removed (Gonzalez and Woods, 2007). To find the size of the structuring element for closing operation, one micropad pixel edge length must be determined. One micropad pixel edge length was estimated manually and used as a parameter for closing. The result of closing was a gray scale image (Fig. 2c). To convert it to a binary image, Otsu's Threshold method was applied (Smith et al., 1979). As a result, a binary image, $\boldsymbol{B_p}$, that has only micropads is obtained (Fig. 2d).

3.2. Bead detection and quantification

Main steps of immunomagnetic bead detection and counting steps are depicted in Fig. 3.

Beads generally have regular circular shape. However, if they attract to each other and form a cluster, the cluster shape is not uniform. Besides, micropads may overlap and cover some part of the beads, in that case beads lose their circular shape. As it is mentioned early, beads might join to each other because of magnetization. It was reported that micron size superparamagnetic beads show higher hysteresis than nano size superparamagnetic beads of the same material (Duriagina et al., 2018). Also, we did not employ any Faraday Cage to block the external magnetic fields in the environment. In our previous work, we showed that the line formation of magnetic beads is due to external magnetic field (Mzava et al., 2016b). Consequently, we decided that when the accumulation of beads is along a line, it was due the magnetization.

Beads are also significantly opaquer than cells. Since our main purpose is to detect cells, we can also detect and remove beads by taking those distinctive features into consideration. To eliminate beads from the images, mainly, filtering, thresholding, segmentation and morphological operations were mainly applied. However, another purpose of this work is to find the amount of the beads in the image, so we need an image only consists of beads. Quantifying the number of beads can help to determine and optimize the initial concentration of added beads. In the case of excessive number of unbound beads in the microfluidics, the initial concertation of beads for immunomagnetic separation step can be reduced. Initially, on the image, micropads and beads were identified together. To detect beads, which are attached to micropads, borders of micropad and beads were recognized. In addition, to quantify total number of beads, borders of each bead were identified. For those cases, watershed algorithm was implemented (Meyer, 1994). Instead of applying watershed algorithm on the original RGB image, RGB was first converted to a gray-scale image, $\boldsymbol{I_{gray}}$, then to clear noises Gaussian filter with 3 pixels (in both x and y directions) as the standard deviation of the Gaussian distribution was applied, finally Otsu' Threshold method was employed.

$$\boldsymbol{I_{mask}}(\boldsymbol{x},\boldsymbol{y}) = \begin{Bmatrix} 1, & \text{if } \tau_{otsu} > \boldsymbol{I_{gray}}(\boldsymbol{x},\boldsymbol{y}) \\ 0, & \text{if } \tau_{otsu} < \boldsymbol{I_{gray}}(\boldsymbol{x},\boldsymbol{y}) \end{Bmatrix} \tag{1}$$

In Eq. (1), τ_{otsu} was the threshold value which was found by using Otsu's Threshold algorithm, and $(\boldsymbol{x},\boldsymbol{y})$ is the pixel position in the image. The binary image $\boldsymbol{I_{mask}}(\boldsymbol{x},\boldsymbol{y})$ had only micropads and immunomagnetic beads. Before applying the watershed algorithm only to immunomagnetic beads and micropads, gray-scale image of the original image was masked with $\boldsymbol{I_{mask}}(\boldsymbol{x},\boldsymbol{y})$. At the end of this step, gray-scale image contains only immunomagnetic beads and micropads and everything else including background were black, $\boldsymbol{I_{masked}}$. After generating the $\boldsymbol{I_{masked}}$, by applying the Otsu's Threshold, binary image with bead and micropad, $\boldsymbol{B_{bp}}$, was obtained. Then a distance map ($\boldsymbol{I_{distance}}$) was generated. For the distance measurement, Euclidean method was implemented (Danielsson, 1980). After that, by using watershed segmentation objects in the image were labeled (O_l).

$$O_l \longleftarrow \text{Watershed } (I_{distance}) \tag{2}$$

In Eq. (2), $\boldsymbol{l} = \{1,2,\ldots,N\}$ shows index of the labeled objects. The purpose of the watershed segmentation was demarcating between

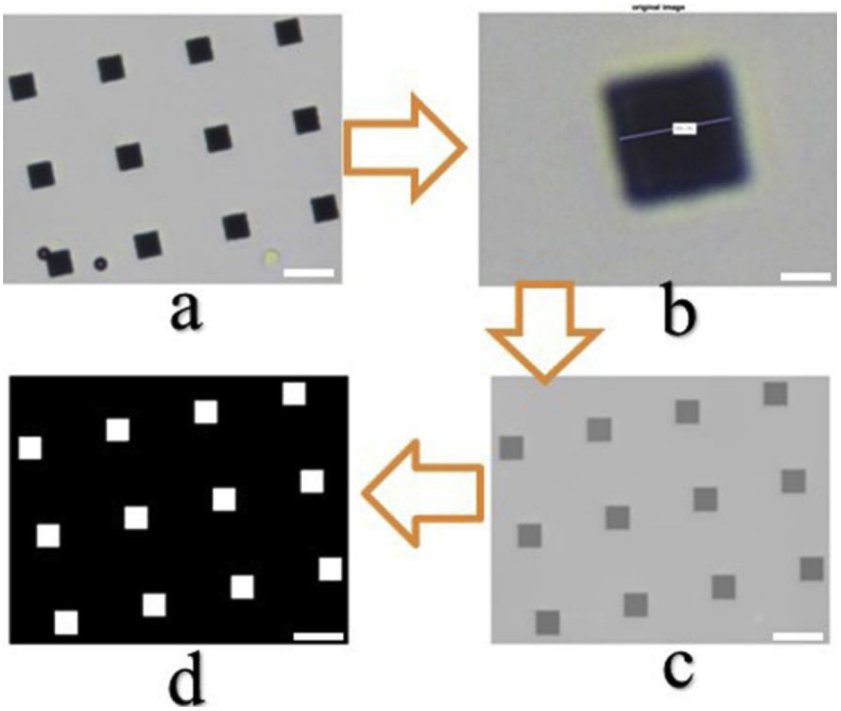

Fig. 2. a) Original RGB image, b) a micropad from the original image, c) result of micropad extraction algorithm, image is in gray-scale, and d) binary image obtained by using Otsu's threshold on gray-scale image in c. Scale bars = 20 μm.

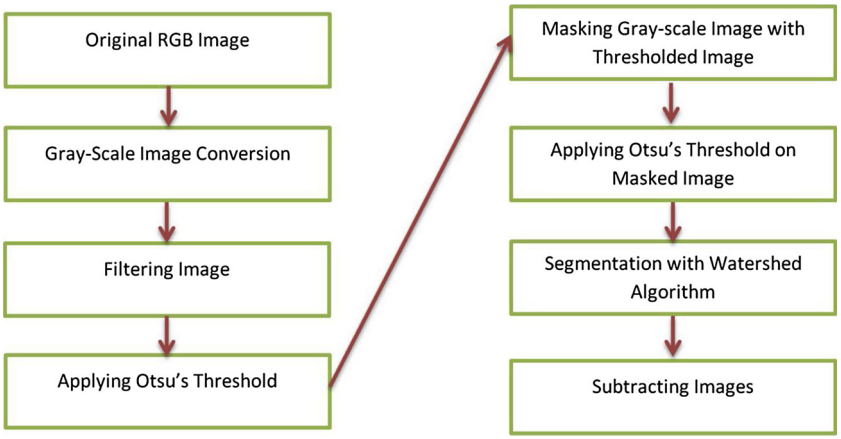

Fig. 3. Flow diagram of immunomagnetic bead detection and quantification steps.

objects which were appeared as combined in the image. After that, to be able to obtain only beads on image, $\boldsymbol{B_p}$ was subtracted from the O_l. Final image only contained beads, $\boldsymbol{B_b}$, was in binary format. Images during each step of Fig. 3. are shown in Fig. 4.

3.3. Cell detection and quantification

Cells have irregular shapes and sizes in the image. They may present as a single cell, bounded to single bead or more beads, bounded to micropads or bounded to both beads and micropads together. Here our main purpose was to detect only the cells in the image. Initially, variance matrix of the original RGB images that was converted to double format was found using Eq. (3). Window size for calculating the variance matrix was determined to be 11 as a result of a trial and error process. Variance matrix detected the edge of each object on the background (Variance, 2020).

$$V_w = \frac{1}{N-1}\sum_{i=1}^{N} |A_{w(i)} - \mu|^2 \quad (3)$$

Where A_w was a small size matrix made up of N scalar observations, and μ was the mean of A_w. To be able to identify cells, immunomagnetic beads and micropads on the variance matrix clearly, threshold value was applied to the matrix. The threshold value was 2.7x 10^{-4} and image segmenter tool was used to determine the optimum threshold by a trial and error process (Image Segmentation Using the Image Segmenter App - MATLAB and Simulink, 2020). Then, binary image which contains cells, micropads and immunomagnetic beads, B_{cbk}, was obtained. After that, our aim was to remove immunomagnetic beads and micropads from the image, and obtain an image consisting of only cells.

3.3.1. Bead and micropad detection for cell finding steps

During the bead detection step, after the watershed segmentation, segmented beads, micropads and some cell pieces, which are similar to

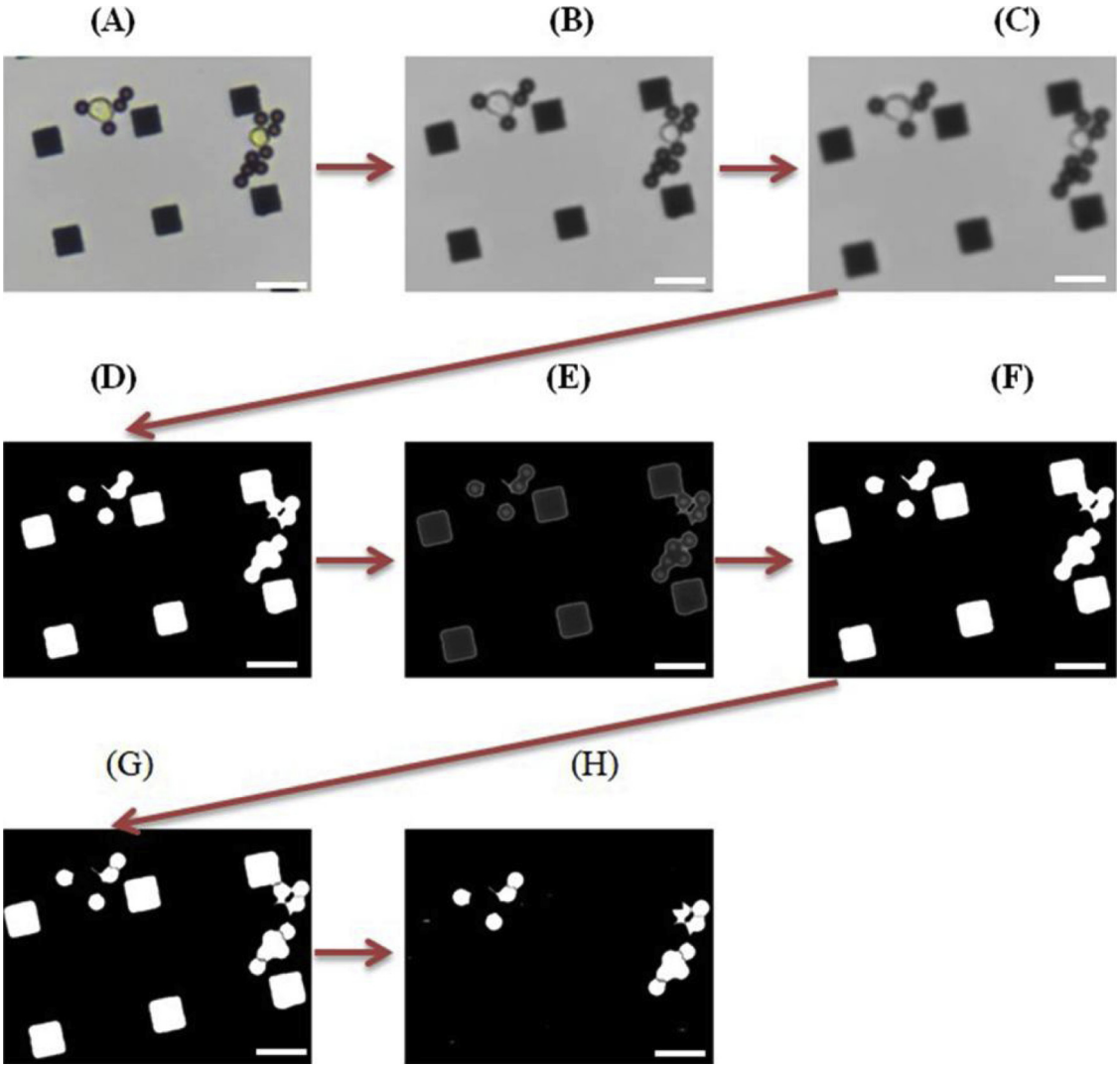

Fig. 4. (A)Original RGB image, (B) gray-scale image, (C) filtered image, (D) binary image after Otsu's threshold, (E) masked gray-scale image, (F) binary image of masked image after Otsu's threshold, (G) binary image after watershed segmentation, and (H) binary micropad subtracted image. Scale bars = 20 μm.

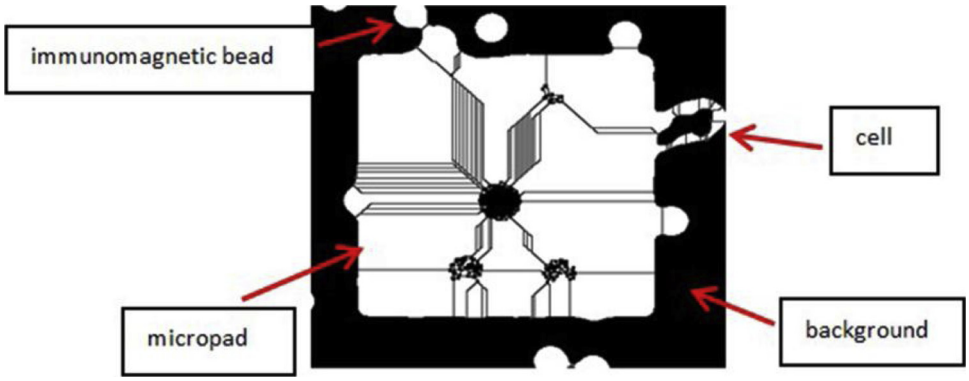

Fig. 5. Result of the watershed algorithm. In the image there are some cells, micropad and immunomagnetic beads. Background is black. Watershed lines are visible between different objects and even in the same object.

beads and micropads, are obtained (Fig. 5). It can be seen from the Fig. 5 that some cell parts are visible. If this segmented image was directly used to subtract bead and micropad from the B_{cbk} image, detection of some cell parts can be missed. Thus, before subtraction, cell pieces should be cleared from the image.

To remove cell portions, like in Fig. 5, opening operation was employed. However, direct application of the opening operation to the result of O_l caused some parts of the micropads to remain in cell only image. To overcome this situation, after the watershed, $\boldsymbol{B_p}$ image was added to O_l. Then, morphological opening operation was applied while the opening parameter was set to 225 which is the half of the pixel area of the immunomagnetic bead. As a result of these steps, some noise signals, pieces of immunomagnetic beads and cells were cleared from the O_l. The final image was called as B_s, and dilation operation was

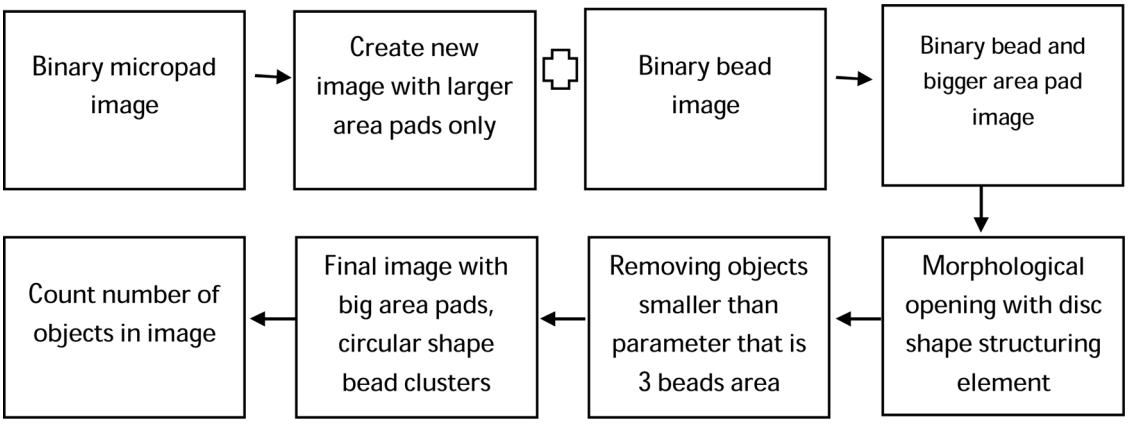

Fig. 6. Flow diagram of cluster finding and counting steps.

applied on it. Then the image was subtracted from the binary image that had cells, beads, and micropads, B_{cbk}, and cell only image, B_c, was procured as:

$$\widehat{\mathrm{B}}_{\mathrm{C}} = B_{cbk} - (B_s \oplus \mathrm{s}) \tag{4}$$

Where $\oplus$ was the dilation operation, and s was a disc shaped structuring element.

Next, in the cell images to clear noises, morphological operations were applied. After this step, the resulted image was in binary format, and contained only the cells, in order to count the number of cells, objects were traced (Gonzalez and Woods, 2007).

3.4. Cluster detection and quantification

The cluster detection steps are shown in Fig. 6. A larger micropad denotes that cells and beads were attached to the micropad and formed a cluster on the micropad. To detect this clusters, by using $\boldsymbol{B_p}$, the areas of larger micropads were identified, and a new image was created. Then this image was added to $\boldsymbol{B_b}$ image. After that, to find clusters which were formed by beads, first opening operation with disc was applied to obtain the circular shapes of bead colonies (when beads form cluster around a single cell, the cluster shape becomes almost circular). Next, small objects, which are not clusters, were removed. Finally, on the original image, larger micropads, circular shaped and certain size bead clusters were remained. Then, binary operations of object detection and counting were performed.

3.5. Detection of cell and cluster attached to the micropads

The micropads in the microfluidic biochip were functionalized with CD45 antibody using the methods presented in [22.] In the biochip if the cells have CD45 antigen on the cell membrane, micropads capture these CD45+ cells. This means that, the quantification of cells or clusters attached to the micropads reveal information about the immunophenotype of the cells. To analyze the cells attached to micropads, after cell, micropad and cluster detection steps, following method was implemented.

B_p was dilated by morphological operation in Eq. (5).

$$\mathrm{D}_p = \mathrm{B}_p \oplus \mathrm{Se} \tag{5}$$

Where Se was square shaped structuring element and $\oplus$ was binary dilation operation.

B_c was eroded by the morphological operation in Eq. (6).

$$E_c = \widehat{\mathrm{B}}_{\mathrm{C}} \ominus \mathrm{SE} = \{\mathrm{z} | (SE_z \subseteq B_c)\} \tag{6}$$

Where SE was disc shaped structuring element and $\ominus$ was binary erosion operation. In other words, the result of erosion operation was obtained by identifying perfect overlaps between the structuring element (SE) with the foreground pixels in B_c and translating the set of pixel locations to z matrix.

Then, dilated micropad image, eroded cell image and binary cluster were compounded. After that, morphological closing operation was applied and, C_{cp}, image was created. After that, object finding on binary image by using connected component algorithm was performed. Then, in B_p, area of a micropad was calculated and C_{cp} was scanned to find the larger micropads. This means that, if an object area was larger than the area of one micropad, cells or clusters were attached to the corresponding micropad. With this way, cells or clusters bonded to the micropads and their locations were obtained and counted.

4. Results

The images were recorded at different time and for each image, the number of cells, immunomagnetic beads, micropads and cells captured on the micropads were counted by using the proposed algorithm. In addition, the results of the algorithm were compared with manual counting and flow cytometry results. We had two different image sets to test the algorithm; cells from the cell culture and patient cells. To show the potential of the algorithm, 75 real patient images from 4 different patients at different days were analyzed. All the patients responded to chemotherapy and the number of blast cells were reduced on the following days of the chemotherapy. The developed algorithm was able to reveal the similar output with the manual counting and flow cytometry. In order to determine the performance of the proposed algorithm, true positive, false positive, and false negative values were found and by using them, precision, recall, F-measure, absolute percentage error were calculated (Chiang et al., 2018; Kumar et al., 2015).

4.1. Quantification of micropads and immunomagnetic beads

In an image, micropads are uniform in size, but in different biochips micropads with different sizes were tested. Micropads were detected with less error rate as a result of their regular shape and size. Also, for each image a single immunomagnetic bead had uniform shape and size but accumulation of immunomagnetic beads had nonuniform shapes and sizes which required extra processing steps. However, the proposed algorithm was able to identify immunomagnetic beads, their location and quantity. For both immunomagnetic bead and micropad finding, error rate is identified to estimate the accuracy of the algorithm. Error rate is given by Eq. (7) (Uslu et al., 2019).

$$E = \left| \frac{\widetilde{N} - N}{N} \right| \tag{7}$$

Where N is number of micropads or beads, $\widetilde{N}$ is number of micropads

Table 1
Average bead and micropad detection and counting performance results.

Average TP	Average FP	Average FN	Precision	Recall	F-Measure	APE	Detection Error
9.38	2.09	1.76	0.81	0.84	0.82	2.94	0.17

or beads found by the proposed algorithm. Error rate for micropad detection was 0.01 while error rate for bead detection was 0.02.

4.2. Quantification of cells and clusters attached to the micropads

In the experiments, micropads with different sizes (e.g. 15 μm x 15 μm, 24 μm x 24 μm, 35 μm x 35 μm) were tested. The size of the micropad effects the accuracy of detecting cells and accuracy of detecting clusters attached to the micropads. If the micropad size is small (15 μm x 15 μm), cells and beads do not overlap with the micropads and they can be identified with higher precision. On the other hand, if the micropad size is larger (35 μm x 35 μm), cells and beads cannot be seen clearly and so, it is difficult to detect them. In Table 1, average result by using whole 75 images are given.

From Table 1 it can be seen that, precision, recall and F-measure values are higher than 80 %.

4.3. Quantification of cells

In an image, cells may appear in different forms such as isolated cell, partially covered cell or fully covered cell. Partially and fully covered cell refers to cells that are bound to immunomagnetic beads. The detection of partially or fully covered cells requires extra computation steps, and after detecting cells for different forms, the results were combined to calculate the overall number of cells.

Before examining the patient samples, we used cell culture samples to test the proposed algorithm. Average results of cell culture samples were given in Table 2. The cells in the cell culture had higher uniformity and bigger size compared to patient samples, thus, higher precision and recall rate for cell culture images were obtained.

4.3.1. Detection of partially covered and isolated cells

Compared to cell clusters, isolated and partially covered cells have visible cell parts. This means that, a different approach was needed to detect partially covered and isolated cell detection. In Table 3, it can be seen that, recall level reaches 90 % success. This indicates that most of the cells are detected correctly, while there is a low number of missed detections.

4.3.2. Detection of fully covered cells (clusters)

When many immunomagnetic beads were bound to a single cell, the cell was not visible and the cell counting algorithm alone did not detect the cell. However, even if a cell is not visible directly, there might be a cell under the beads and it must be counted as a cell. Those covered cells are called as cluster, and there are different methods than cell detection and counting process to identify clusters since they are in a different form compared to a single cell which can be recognized using the features, such as, color, shape, and size. In this work, we also checked the size of clusters and evaluated how many cells would present in the cluster. The immunomagnetic beads are 4.5 μm in diameter, when cells are fully covered with immunomagnetic beads, the size of the cluster is approximately 20 μm (Fig. 1c red arrow). Larger-size clusters can be determined as multiple cells based on the size of the cluster (Fig. 1b red arrow).

The average precision was 93 %, and the average F-measure was 85 % for all dataset (Table 4). High precision means that most of the clusters are detected correctly, and there are only few incorrect detections.

4.3.3. Cell detection and quantification for patient dataset

In Fig. 7 cell detection results for patient images are shown. Different patient samples on different days, were analyzed using the proposed algorithm. It can be seen that micropad sizes may change, and also clarity of the image may change depending on the micropad size, illumination effect, color change, and immunomagnetic bead intensity. If micropad sizes were small and, cells were clear on the image, then the algorithm could reach as an average more than 95 % precision rate. In addition, when the micropad sizes were large, and bead intensity was low we were able to obtain high precision. If these conditions were satisfied, as an average more than 90 % precision was obtained. Since large micropad size resulted in the covering of cells and beads, identifying cells and clusters became more challenging. In Fig. 7 results show both bead cluster and cell detection. The images were recorded by different personal and light settings of the microscope were adjusted individually resulting in brightness and color variations for images. Even the images were very different from each other, cells were found with an average 85 % precision, and an average 86 % recall value.

In this study, 12 samples from 4 different patients were processed and the relevant chip images were acquired. For each patient different time samples for the diagnosis, 15th. day, 90th. day, etc. were collected due to the availability of the patients and the medical center. Also, different size micropads were tested to investigate the impact. The size of the micropads directly affected the results of the developed algorithm. If the micropad area was larger, lower precision was obtained. The proposed algorithm is applied to all of 75 images, each image is 4067-pixel x 3116-pixel represents 540 μm x 720 μm area of the chip surface. For one sample, minimum 3 images (maximum 12 images) at different locations of the chip were analyzed and the average number of cells in one image was calculated. The images of the chip surfaces that did not have any cells were excluded. A medical expert manually counted the cells under microscope and the overall results are shown in Fig. 8. As an expected result of applied chemotherapy, the number of blast cells should decrease on the 15th day compared to the instant of diagnosis. On the following days after the 15th day, the number of healthy cells with CD45 antigen on the cell surface increase and the obtained trends are mostly in good agreement with the literature reporting the changes of cell numbers during the treatment (Nagant et al., 2018). As shown in Fig. 8, the trend of manual and automated counting was highly similar.

In this manual and automated counting comparison study, since there were two independent groups, and there were limited number of samples, non-parametric Mann-Whitney *U* test was used to investigate their statistical relation (Kasuya, 2001). For the test we had two hypothesis; H_0 : Statistically there is no difference between manual

Table 2
Cell culture experiments: Average cell counting performance results for 20X objectives.

	Average TP	Average FP	Average FN	Precision	Recall	F-Measure	APE	Detection Error
20X objective	134.5	1.3	2.3	0.99	0.98	0.98	−0.73	0.01

Table 3
Average cell counting performance results for partially covered and isolated cells.

Average TP	Average FP	Average FN	Precision	Recall	F-Measure	APE	Detection Error
11.41	3.75	1.18	0.75	0.90	0.82	20	0.17

Table 4
Average cell counting performance results for fully covered cells.

Average TP	Average FP	Average FN	Precision	Recall	F-Measure	APE	Detection Error
4.24	0.29	1.10	0.93	0.79	0.85	−15.15	0.13

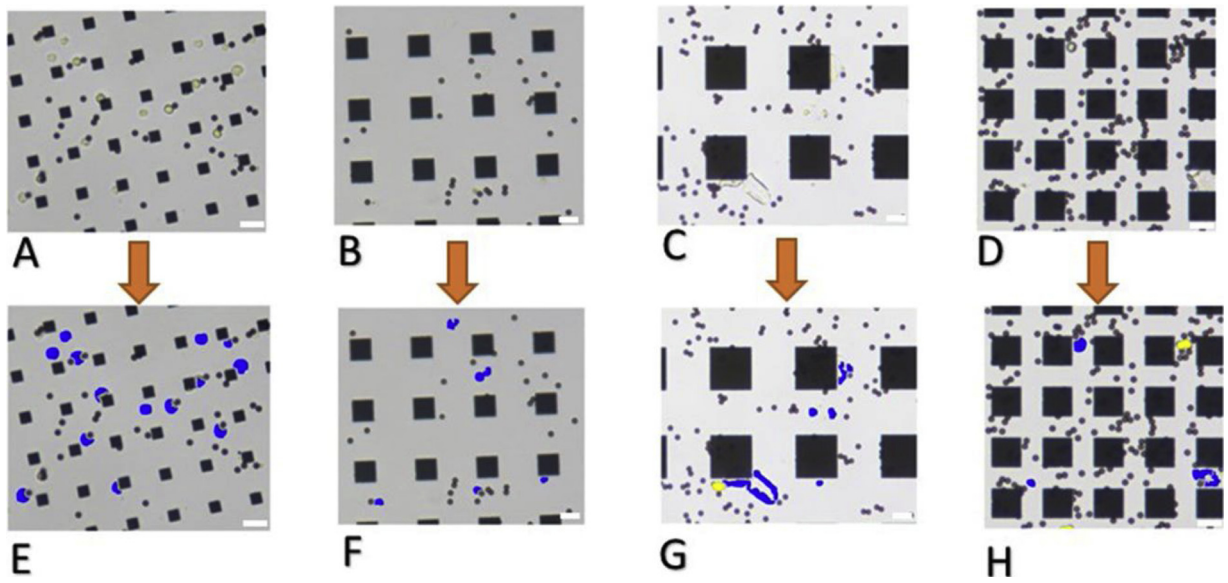

Fig. 7. Cell detection and quantification result examples. Images belong to different patient along with different day. Blue color shows detected cells while yellow color shows detected clusters. Given images are some parts of the whole images. A, B, C, and D are original RGB images, E, F, G, and H are final result images. Scale bars = 20 μm (For interpretation of the references to colour in this figure legend, the reader is referred to the web version of this article.).

counting and automated counting, H_1: Statistically there are differences between manual counting and automated counting. When the test was completed with all 4 patients separately, patient 1, patient 2, patient 3, patient 4 had 0.87, 0.51, 0.12, 0.56 Asymp. Sig. values respectively. This means that all four values were bigger than 0.05, hypothesis H_0 was retained, and concluded that there was no statistically significant difference between manual counting and automated counting.

The smallest Asymp. Sig value was calculated for patient 3, and in Fig. 8 even though the trends were similar the average number of cells obtained from the manual counting and automated counting deviated more compared to the results for the other patient samples. The main reasons of this deviation were 1) using larger micropads (35 μm x 35 μm) for this patient, and 2) the intensity of the micropads were higher compared to other images. When micropads overlapped and blocked the visibility of the cells, the proposed algorithm could not detect every cell in the image. For the patient 1, small size micropads (15 μm x 15 μm) were used and cells were not blocked by the micropads in the image, as a result automated cell counting yielded similar numbers with manual counting.

5. Conclusion

The proposed algorithm is aimed to be used to detect and count cells in a biochip. The biochip includes immunomagnetic beads and micropads for separation of the target B lymphoblast cells. For this study main image objective was 20 × . Without cell staining, color, size and shape-based methods achieved 85 % precision and 86 % recall and F-measure for patient dataset. To test proposed methods, precision, recall, f-measure, absolute percentage error and detection error rate was used. The results show that even if micropad size and bead density change, our algorithm can find cells. In addition, although micropad size may differ, micropads can be found with high accuracy. If micropad size is small on the image, cells can be seen clearly, then the cell quantification yields better results on those images. The highest precision and recall are 98 % for the clear images of cultured cells (analyzed with small micropads) shows the power of the developed method. In addition, proposed algorithm detects beads and micropads on the image with 0.02 and 0.01 detection errors respectively. When determining the performance of the algorithm such as precision, recall, F-measure and others, we compared the outputs of the algorithm with the output of our manual evaluation of the images. On the other hand, for the patient samples the statistical test compared the outputs of the algorithm with the outputs of the medical expert's evaluation of the chips. The statistical test revealed that the manual counting of the medical expert and automated counting are statistically in good agreement.

6. Discussion

In order to separate and visualize cells in images cells are stained (Ounkomol et al., 2018). Breast cancer associated cytokeratin positive cells were separated from blood by using immunomagnetic beads and immunocytochemically stained for cell detection (Witzig et al., 2002). In our proposed method, detecting immunomagnetic beads has two purposes that are inherent cell separation feature and being visual

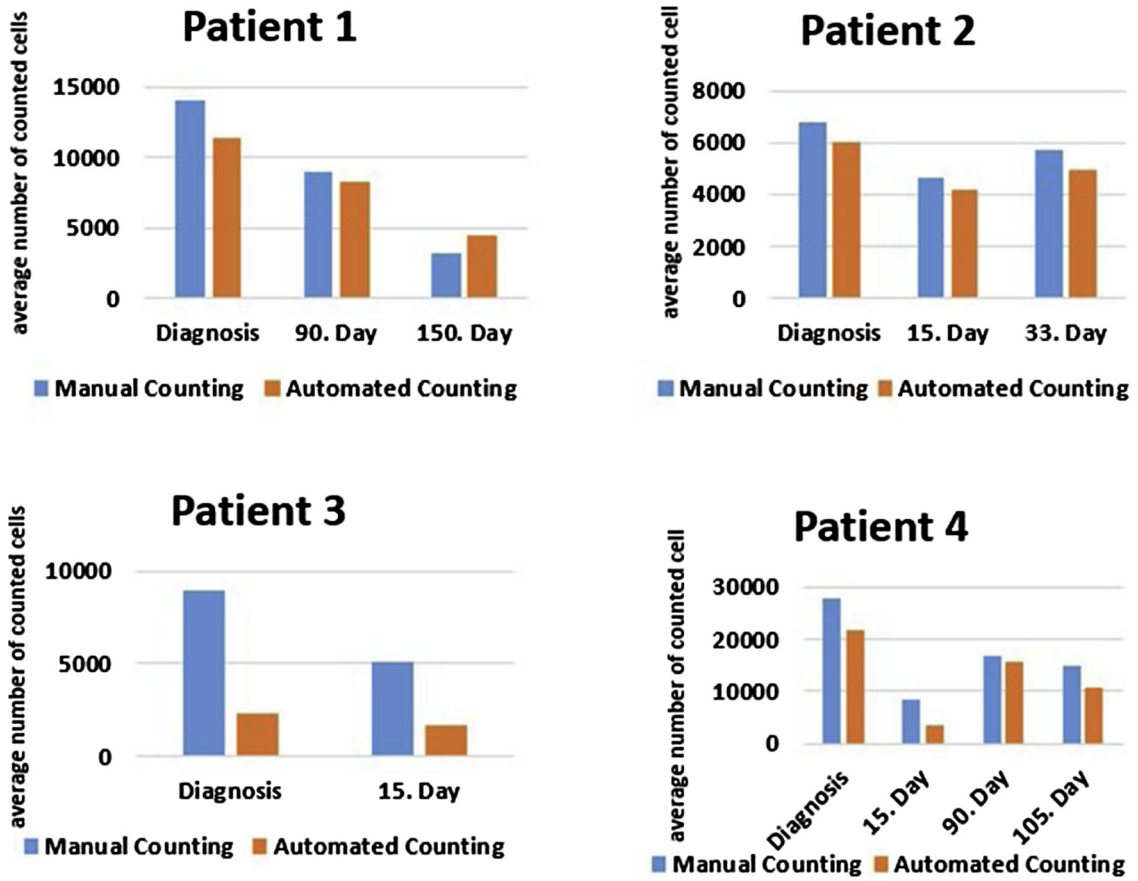

Fig. 8. Results of proposed algorithm on different patients. Each graph shows comparison of manual counting and automated counting for different patient.

markers for cell detection.

Detection of cells from microscopy images are reported in (Mohapatra et al., 2010) with 95 % accuracy, in (Patel and Mishra, 2015) with 93.4 % accuracy, and in (Ghane et al., 2017) with 97 % precision. However, those cells are stained by using violet color that makes cell distinctive. On the other hand, in our method cells are not stained and average precision and recall rates are more than 85 % on for all patient samples. Reducing the micropad size resulted in 95 % precision and 97 % recall.

In this study, the images include not only cells but also immunomagnetic beads and square micropads which create more challenging cases as distinct from cell analysis in (Long et al., 2006; Mualla et al., 2013). We developed automated image processing methods to solve five problems: cell detection, cluster detection, bead detection, micropad detection and cell or cluster attached micropad detection, and then to quantify cells. We developed simple but fast and effective detection algorithms and tested them on two types of datasets; the cell culture and the patient samples. Proposed method gives higher precision rate on the cell culture than patient image because cells are clearer in cell culture, and also in some patient images micropads are very large, and it is difficult to identify cells on those images.

In our previous study (Uslu et al., 2019) since cells were not clear, and this made cell detection more challenging, we used machine learning and more complex algorithms. Total algorithm run time was more than 300 s. However, in this study, existence of micropads in the images added one more complexity. Also, the developed algorithm will be the signal readout method of the biochip's real time measurements which requires lower run times. In order to analyze more complicated images in a lower run time (average run time was 90 s) we preferred relatively simple image processing techniques and not machine learning algorithms.

The developed system incorporated color, size and shape-based methods to identify the cells, immunomagnetic beads and micropads. Even though the cells were magnetically separated from complex bodily fluid and then introduced to the microfluidics, there might be some artifacts in the microfluidics. Size, color and shape-based filters can be simply added to the algorithm to identify the artifacts. For example, the larger size cell in Fig. 7c and 7 g has a circler and non-circler parts and a total length of approximately 31 μm. The developed algorithm identified it as 2 cells, but it is possible by adding shape and size filters to identify the circler part as a cell and identify the non-circler part as an artifact. The immunomagnetic separation has high yield (95–98 % (İçöz et al., 2019)) of capturing target cells and our platform was developed based on this fact. However, as a scenario if non-target cells present in the microfluidics which are similar size of the target cells, the current algorithm is not able to distinguish between non-target and target cells.

Different micropad sizes were used for the patient samples collected on different dates after the chemotherapy started. In some tested biochips micropads have larger area and this makes detection and quantification of the cells difficult. In some samples, the size of micropads were reduced (15 μm x 15 μm) thus we obtained better cell detection results. As a future work, we will test smaller micropads in order to find the optimum size for patient samples, the micropads should not block and shadow any cells but they also have sufficient surface area for capturing cells.

In (Wang et al., 2018) and (Georg et al., 2018) Python based image processing methods are used to identify biomedical and chip images. They claim that python makes modern computer algorithms easier to be applied in bioimage analysis. As future work, we are also planning to study on Python based image processing techniques and compare them with our results.

Declaration of Competing Interest

The authors declare that they have no known competing financial interests or personal relationships that could have appeared to influence the work reported in this paper.

Acknowledgement

Authors acknowledge TÜBİTAK (Project No: 115E020) for financial support and Ünal Akar for fabricating and preparing biochips.

References

Böttcher, S., et al., 2008. Minimal residual disease detection in mantle cell lymphoma: methods and significance of four-color flow cytometry compared to consensus IGH-polymerase chain reaction at initial staging and for follow-up examinations. Haematologica.

Chiang, P.J., Wu, S.M., Tseng, M.J., Huang, P.J., 2018. Automated bright field segmentation of cells and vacuoles using image processing technique. Cytom. Part A 93 (10), 1004–1018.

Danielsson, P.E., 1980. Euclidean distance mapping. Comput. Graph. Image Process. 14 (3), 227–248.

De Chaumont, F., et al., 2012. Icy: an open bioimage informatics platform for extended reproducible research. Nat. Methods 9 (7), 690–696.

DeSantis, C.E., et al., 2014. Cancer treatment and survivorship statistics, 2014. CA Cancer J. Clin. 64 (July(4)), 252–271.

Duriagina, Z.A., Tepla, T.L., Kulyk, V.V., 2018. Evaluation of Di erences between Fe3O4 micro- and nanoparticles properties. Acta Physica Polonica A.

Faley, S., et al., 2008. Microfluidic platform for real-time signaling analysis of multiple single T cells in parallel. Lab Chip.

Gao, B., Klumpen, H.J., Gurney, H., 2008. Dose calculation of anticancer drugs. Expert Opin. Drug Metab. Toxicol.

Georg, M., et al., 2018. Development of image analysis software for quantification of viable cells in microchips. PLoS One 13 (3), 1–15.

Georgantzoglou, A., et al., 2015. Automatic cell detection in bright-field microscopy for microbeam irradiation studies. Phys. Med. Biol. 60 (16), 6289–6303.

Ghane, N., Vard, A., Talebi, A., Nematollahy, P., 2017. Segmentation of white blood cells from microscopic images using a novel combination of K-Means clustering and modified watershed algorithm. J. Med. Signals Sens. 7 (2), 92–101.

Gonzalez, R.C., Woods, R.E., 2007. Digital Image Processing, 3rd edition. .

Hauwel, M., Matthes, T., 2014. Minimal residual disease monitoring: The new standard for treatment evaluation of haematological malignancies? Swiss Med. 144.

Hazwani, N., Halim, A., Mashor, M.Y., Hassan, R., 2011. Automatic blasts counting for acute leukemia based on blood. Int. J. Res. Rev. Comput. Sci. 2 (4), 971–976.

Icoz, K., Soylu, M.C., Canikara, Z., Unal, E., 2018. Quartz-crystal microbalance measurements of CD19 antibody immobilization on gold surface and capturing B lymphoblast cells: effect of surface functionalization. Electroanalysis 30 (5), 834–841.

İçöz, K., Gerçek, T., Murat, A., Özcan, S., Ünal, E., 2019. Capturing B type acute lymphoblastic leukemia cells using two types of antibodies. Biotechnol. Prog. 35 (1).

"Image Segmentation Using the Image Segmenter App - MATLAB & Simulink".

Jackson, J.M., et al., 2016. Microfluidics for the detection of minimal residual disease in acute myeloid leukemia patients using circulating leukemic cells selected from blood. Analyst.

Kasuya, E., 2001. Mann-Whitney *U* test when variances are unequal. Anim. Behav. 61 (6), 1247–1249.

Kumar, R., Srivastava, R., Srivastava, S., 2015. Detection and classification of Cancer from microscopic biopsy images using clinically significant and biologically interpretable features. J. Med. Eng. 2015, 1–14.

Li, K., Chen, M., Kanade, T., 2007. Cell population tracking and lineage construction with spatiotemporal context. Lect. Notes Comput. Sci. (including Subser. Lect. Notes Artif. Intell. Lect. Notes Bioinformatics) 4792 LNCS (PART 2), 295–302.

Long, X., Cleveland, L., Lawrence Yao, Y., 2006. Automatic detection of unstained viable cells in bright field images using a support vector machine with an improved training procedure. Comput. Biol. Med. 36 (4), 339–362.

Masdor, N.A., Altintas, Z., Tothill, I.E., 2017. Surface plasmon resonance immunosensor for the detection of Campylobacter jejuni. Chemosensors.

Mata, G., et al., 2019. Automated neuron detection in high-content fluorescence microscopy images using machine learning. Neuroinformatics 17 (2), 253–269.

Meyer, F., 1994. Topographic distance and watershed lines. Signal Processing.

Mohapatra, S., Patra, D., Satpathi, S., 2010. Image analysis of blood microscopic images for acute leukemia detection. 2010 Int. Conf. Ind. Electron. Control Robot. IECR 2010 215–219.

Mualla, F., Scholl, S., Sommerfeldt, B., Maier, A., Hornegger, J., 2013. Automatic cell detection in bright-field microscope images using sift, random forests, and hierarchical clustering. IEEE Trans. Med. Imaging 32 (12), 2274–2286.

Mzava, O., Tas, Z., İçöz, K., 2016a. Magnetic micro/nanoparticle flocculation-based signal amplification for biosensing. Int. J. Nanomedicine 11, 2619–2631.

Mzava, O., Taş, Z., İçöz, K., 2016b. Magnetic micro/nanoparticle flocculation-based signal amplification for biosensing. Int. J. Nanomedicine 11, 2619–2631.

Nagant, C., Casula, D., Janssens, A., Nguyen, V.T.P., Cantinieaux, B., 2018. Easy discrimination of hematogones from lymphoblasts in B-cell progenitor acute lymphoblastic leukemia patients using CD81/CD58 expression ratio. Int. J. Lab. Hematol.

Neale, G.A.M., et al., 2004. Comparative analysis of flow cytometry and polymerase chain reaction for the detection of minimal residual disease in childhood acute lymphoblastic leukemia. Leukemia 18 (5), 934–938.

Ounkomol, C., Seshamani, S., Maleckar, M.M., Collman, F., Johnson, G.R., 2018. Label-free prediction of three-dimensional fluorescence images from transmitted-light microscopy. Nat. Methods 15 (11), 917–920.

Padfield, D., Rittscher, J., Thomas, N., Roysam, B., 2009. Spatio-temporal cell cycle phase analysis using level sets and fast marching methods. Med. Image Anal. 13 (1), 143–155.

Patel, N., Mishra, A., 2015. Automated leukaemia detection using microscopic images. Procedia Computer Science, vol. 58. pp. 635–642.

Putzu, L., Caocci, G., Di Ruberto, C., 2014. Leucocyte classification for leukaemia detection using image processing techniques. Artif. Intell. Med. 62 (3), 179–191.

Schindelin, J., et al., 2012. Fiji: an open-source platform for biological-image analysis. Nat. Methods 9 (7), 676–682.

Smith, P., Reid, D.B., Environment, C., Palo, L., Alto, P., Smith, P.L., 1979. Otsu_1979_otsu_method. C, no. 1. pp. 62–66.

Sun, W., et al., 2018. Outcome of children with multiply relapsed B-cell acute lymphoblastic leukemia: a therapeutic advances in childhood leukemia & lymphoma study. Leukemia.

Tse, S., Bradbury, L., Wan, J.W.L., Djambazian, H., Sladek, R., Hudson, T., 2009. A combined watershed and level set method for segmentation of brightfield cell images. Med. Imaging 2009 Image Process 7259 (March 2009) p. 72593G.

Uslu, F., Icoz, K., Tasdemir, K., Yilmaz, B., 2019. Automated quantification of immunomagnetic beads and leukemia cells from optical microscope images. Biomed. Signal Process. Control 49 (March), 473–482.

Variance - MATLAB var.

Wang, A., Yan, X., Wei, Z., 2018. ImagePy : An Open-Source, Python-Based and Platform-Independent Software Package for Bioimage Analysis. vol. 34, no. April. pp. 3238–3240.

Witzig, T.E., et al., 2002. Detection of circulating cytokeratin-positive cells in the blood of breast cancer patients using immunomagnetic enrichment and digital microscopy. Clin. Cancer Res. 8 (5), 1085–1091.

Xing, F., Yang, L., 2016. Robust nucleus/cell detection and segmentation in digital pathology and microscopy images: a comprehensive review. IEEE Rev. Biomed. Eng. 9, 234–263.